

Role of orbital selectivity on crystal structures and electronic states in BiMnO₃ and LaMnO₃ perovskites

Gheorghe Lucian Pascut^{1,2} and Kristjan Haule¹

¹*Department of Physics & Astronomy, Rutgers University, Piscataway, NJ 08854, USA*

²*MANSiD Research Center and Faculty of Forestry,
Stefan Cel Mare University (USV), Suceava 720229, Romania*

(Dated: December 22, 2024)

Correlated oxides, such as BiMnO₃ and LaMnO₃, show complex interplay of electronic correlations and crystal structure exhibiting multiple first order phase transitions, some without a clear order parameter. The quantitative theoretical description of this temperature dependent electronic-structural interplay in the vicinity of a Mott transition is still a challenge. Here we address this issue by simultaneously considering both structural and electronic degrees of freedom, within a self-consistent density functional theory with embedded dynamical mean field theory. Our results show the existence of novel electronic states characterized by coexistence of insulating, semi-metallic and metallic orbitals. This state is in agreement with resonant X-ray scattering. We also show that electronic entropy plays a decisive role in both electronic and structural phase transitions. By self-consistent determination of both, the electronic state and the corresponding crystal structure, we show that the temperature evolution of these phases can be quantitatively explained from first principles, thus demonstrating the predictive power of the theoretical method for both the structural and the electronic properties.

Manganese oxides with perovskite-type structure host a variety of interesting phenomena, among others the colossal magnetoresistance^{1,2}, insulator to metal transition³, ferroelectricity coexisting with long range magnetic order⁴, and orbital and charge ordering⁵. The theoretical description of these functionalities is challenging, as the electronic correlations play an essential role, and the interplay between the electronic, orbital, and magnetic degrees of freedom with the crystal structure makes these materials extremely sensitive to small changes in external parameters, such as electric voltage, magnetic field, and temperature. However, this high sensitivity is a useful property, which is explored in development of new electronic devices.

The theoretical methods for ab-initio description of strong correlations in solids have been recently developed, and among them the Density Functional Theory with Embedded Dynamical Mean Field Theory (DFT+eDMFT)⁶⁻⁸ has demonstrated predictive power in many classes of correlated materials. For example, it was predicted that the magnetic moment in plutonium metal is screened at 800 K with valence fluctuations⁹, which was subsequently verified by neutron scattering experiment¹⁰. An order of magnitude enhanced electron-phonon coupling in FeSe superconductor as compared to the DFT result was predicted in Ref. 11, and subsequently verified by pioneering experiment using combination of time-resolved photoemission spectroscopy coupled with x-ray diffraction¹². Similarly, prediction of large fluctuating moments in iron superconductors and their energy distribution¹³ have been later verified by neutron scattering¹⁴. The prediction of isostructural metal-insulator transition under pressure in FeO has been confirmed in Ref. 15. Novel type of long ranged order with very high multipole-ordering was proposed to explain the hidden order in URu₂Si₂¹⁶ which was con-

firmed by Raman scattering experiment¹⁷. Finally, structural relaxations by eDMFT method have been recently developed¹⁸ and it was demonstrated on the example of NdNiO₃¹⁹ and Fe₂Mo₃O₈²⁰ that they can predict small changes of crystal structures near the Mott metal-insulators transition, the region which is challenging for other ab-initio methods.

In this paper we study AMnO₃ class of materials with perovskite structure-type to understand the role that correlations play in generating their rich phase diagrams²³⁻²⁶. We compare and contrast LaMnO₃ with BiMnO₃, which have attracted considerable interest due to their giant magnetoresistance phenomena in doped LaMnO₃¹, and potential multiferroic property in BiMnO₃ thin films^{27,28}, respectively.

The high temperature (HT) phase ($T > 800$ K) of both LaMnO₃ and BiMnO₃ is perovskite-type structure with orthorhombic symmetry²⁹⁻³¹ (see Fig. 1a) with similar bad-metallic conductivity^{29,32-34}. At room temperature (RT) both compounds are insulating^{29,35} and in LaMnO₃ the orthorhombic distortions increases with decreasing temperature but the symmetry remains orthorhombic³¹, while in BiMnO₃ the structure distorts to monoclinic symmetry³⁶⁻³⁸. An abrupt change of resistivity is observed in both compounds around the transition, with the high-temperature phase exhibiting nearly temperature independent resistivity, characteristic of a very bad metal. The pattern of structural distortions in both compounds is compatible with the long-range orbital ordering (OO)^{31,36,39,40}, which has been validated by resonant X-ray scattering (RXS) experiments⁴¹⁻⁴³ (see Fig. 1b and c). The theoretical description of this Mott-type transition is most often described within the phenomenological models of cooperative Jahn-Teller (JT) effect due to Mn d^4 configuration in octahedra, leaving a single electron in the e_g shell^{21,24,32,44-47}. However, the two e_g orbitals are

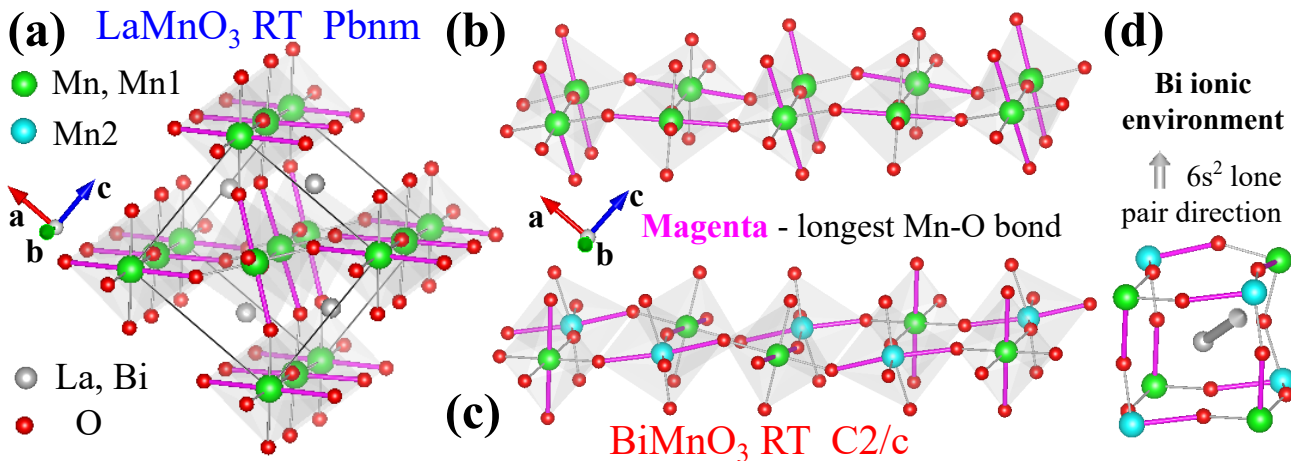


FIG. 1: **Room temperature (RT) structural properties for LaMnO_3 and BiMnO_3 .** (a) schematic view of the crystal structure for LaMnO_3 . The longest Mn-O bond lengths are colored by magenta; (b) displays the octahedra distortion pattern in the (101) plane; (c) distortions in BiMnO_3 in which Mn_1 ions show similar pattern as in LaMnO_3 , while in Mn_2 ions the long-bond distortions are confined to (101) plane; (d) schematic view of Bi environment within a perovskite like crystal structure; the gray arrow, pointing towards the face of the Mn_2O_6 octahedra, shows the direction of the $6s^2$ lone-pair electronic cloud within the Bi ionic environment²¹. The presence of the $6s^2$ lone-pair is responsible for the appearance of two inequivalent Mn sites. Drawings were produced by Vesta²².

not degenerate in the high-temperature metallic phase, therefore the conventional JT mechanism does not apply, and better explanation of the transition is called for. Moreover, experimentally it was found that BiMnO_3 undergoes two phase transitions, a structural phase transition from orthorhombic to monoclinic symmetry takes place at $T = 768\text{ K}$ ²⁹, followed by another isostructural phase transition at $T = 474\text{ K}$ ^{29,36,48}. While orbital order is symmetry allowed at the first transition, RXS experiments showed that the situation is more complicated.⁴³ There is a sharp mean-field type upturn of the forbidden Bragg peak intensity at $T = 768\text{ K}$ followed by the saturation regime. Below the second transition ($T = 474\text{ K}$), there is a second sharp upturn of the intensity, signaling that the long range orbital order is well established only below the second phase transition ($T < 474$). The forbidden Bragg peak intensity in the intermediate phase ($474\text{ K} < T < 768\text{ K}$) saturates to ≈ 0.6 of the room temperature intensity, which suggests that the intermediate phase has some type of partial order, but the nature of this partial order remains unknown. Both transitions are of first order, but the second isostructural transition does not have a clear order parameter.

Mott transition and the Jahn-Teller distortion in LaMnO_3 has been previously studied by Dynamical Mean Field Method using the minimal Hubbard model for the e_g electron, while the t_{2g} electrons were treated semi-classically, as a classical spin S with random orientation.^{49,50} In this approach the effect of covalency is ignored, which was shown by X-ray absorption (XAS) to be important for interpretation of the XAS data⁵¹. Nevertheless, the metal-insulator transition was well cap-

tured by this minimal model approach^{49,50}. In Ref. 49 the transition temperature to disordered state was somewhat underestimated, because the feedback effect of electronic correlations on crystal structure was ignored. This was partially corrected in Ref. 50 by allowing JT distortion, although the full structural relaxation was not attempted. Nevertheless much better estimate for the transition temperature was reported, despite the fact that the electronic entropy was ignored in the calculation of energy. On the other hand, the complex phase diagram of BiMnO_3 has not been theoretically addressed before.

To understand the unusual Mott transition coupled with the partial orbital order from first principles, we use DFT+eDMFT method^{6,8}. Here the downfolding to Hubbard-type models is avoided, and the dynamic correlations are added only to the very localized $3d$ orbitals, which are solution of the Schroedinger equation inside a sphere centered on Mn ion (radius 1.93 bohr). The double-counting between the DFT and DMFT correlations is treated within a nominal scheme⁵². The Coulomb repulsion on these quasi-atomic orbitals used in this work has the Slater form in its fully rotational invariant form with its values estimated by constrained-eDMFT to be $U = 10\text{ eV}$, $J = 1.18\text{ eV}$.

All crystal structures, except the high temperature orthorhombic structure of BiMnO_3 , were experimentally determined^{30,31,36}, and we checked that they agree very well with the theoretically determined optimized crystal structures (see online materials B to E). We note that the force in our approach is calculated from the derivative of the free energy, rather than total energy¹⁸,

therefore it contains important effects of electronic entropy at finite temperature, which we find to be essential to describe orbitally disordered state in the orthorhombic structure, with finite but small orthorhombic distortions. We also note that the high-temperature orthorhombic BiMnO₃ crystal structure has not been determined before, and here is predicted for the first time (see online materials A). It would be desirable to confirm it experimentally.

A schematic view of the room temperature (RT) crystal structure of LaMnO₃ and BiMnO₃ compounds is shown in Fig. 1. It consists of one and two inequivalent corner-sharing MnO₆ octahedra in LaMnO₃ and BiMnO₃, respectively. The two inequivalent octahedra, denoted by Mn₁O₆ and Mn₂O₆, appear due to the lone-pair of electrons derived from Bi 6s orbital²¹, whose direction is shown schematically by the gray arrow in Fig. 1d. Note that the lone-pair consists of electronic charge, occupying the space between the center of Bi and Mn₂ ion²¹, which we mark by the gray arrow.

To describe the Mn 3d orbitals, we use the local coordinate system attached to each Mn ion, in which the hybridization of each orbital with environment is minimal. As expected for octahedral environment, there are three t_{2g} and two e_g orbitals pointing towards the faces and corners of the octahedra, respectively. As shown in Fig. 1d, the lone-pairs are pointing towards the octahedron face of Mn₂ ions, thus for this ion type the t_{2g} orbitals are expected to hybridize with the lone-pair strongly, while the orbitals of Mn₁ ions type, should not directly feel the presence of lone-pair in BiMnO₃.

TABLE I: Occupancy of the Mn orbitals ($n_{e_{g1}}, n_{e_{g2}}$) where $|e_{g1}\rangle \approx |3z^2 - 1\rangle$ and $|e_{g2}\rangle \approx |x^2 - y^2\rangle$. Note that $n_{t_{2g1}} \approx n_{t_{2g2}} \approx n_{t_{2g3}} \approx 1$. The realized electronic states are *band-Mott insulator* (BMI), *orbital-selective Mott* (OSM) state, and *site-orbital-selective Mott* (SOSM) state.

LaMnO ₃	T=300K	T=573K	T=798K
Mn	(0.98, 0.45)	(0.97, 0.46)	(0.76, 0.66)
state	BMI	BMI	OSM
BiMnO ₃	T=300K	T=550K	T=760K
Mn ₁	(0.98, 0.44)	(0.93, 0.47)	(0.72, 0.69)
Mn ₂	(0.98, 0.44)	(0.73, 0.69)	(0.72, 0.69)
state	BMI	SOSM	OSM

While the formal valence of Mn ion is Mn³⁺, our calculation shows that due to covalency there is approximately $n_d \approx 4.4$ electrons on each Mn ion (Mn^{2.6+}), of which almost exactly three electrons are in the t_{2g} shell, and therefore $n_{e_g} \approx 1.4$. This is in good agreement with valence determined from XAS in Ref. 51 ($n_d \approx 4.5$), but it is in stark contrast with the earlier DMFT works in which the number of e_g electrons has been fixed to one electron per Mn.

The degree of the orbital order is usually measured by occupancy ratio $n_{e_{g1}}/(n_{e_{g1}} + n_{e_{g2}}) \equiv (c_2)^2$, which was estimated by neutron scattering to be $c_2 \approx 0.81$ at room

temperature³¹. Table 1 gives the temperature dependence of the occupancies, as found by eDMFT method. We note that the maximal orbital ordering is for $n_{e_{g1}} \approx 1$, but due to covalency $n_{e_{g2}}$ does not vanish in this limit, hence c_2 always remains smaller than 1. In LaMnO₃ we get $c_2 = 0.826$, in good agreement with estimates from Ref. 31. In LaMnO₃ the orbital polarization changes very little as long as the system has sizable charge gap, while orbital polarization becomes very small in the bad-metal phase above $T = 798$ K. Since the two e_g orbitals are not equivalent in the high-temperature structure, there remains a small difference in the occupancy as long as the system is in the orthorhombic phase. We note that in the earlier DMFT work⁴⁹ such agreement with experiment could not be achieved, and it was assigned to negligence of the electron-phonon coupling. In the minimal Hubbard model the insulating state must have integer occupancy, hence the constrained $n_{e_{g1}} + n_{e_{g2}} = 1$ leads to $c_2 \approx 1$ when polarization is large ($n_{e_{g1}} \approx 1$). Hence we now understand that the earlier disagreement with experiment was due to negligence of Mn covalency.

In BiMnO₃ there is an intermediate phase, in which electronic occupancies on the two Mn atoms are very different. Mn₁ keeps orbital polarization close to its room temperature value, while Mn₂ loses its polarization in this temperature range. As we will see later from structural optimization, such results are hard to guess from crystal structure alone, as the Mn₂ octahedra remain quite distorted in this intermediate phase.

If Fig. 2 we show temperature evolution of the density of states (DOS) for both t_{2g} and e_g orbitals. We also display structural information of the experimental structure. Each octahedra has three different types of Mn-O bond-lengths, which are displayed as red horizontal bars. We label them as short ($s \sim 1.9$), medium ($m \sim 2.0$) and long ($l \gtrsim 2.1$). We also provide distortion parameters for octahedra, namely, the *bond distortion index* $\mathbf{D} = \sum_{i=1}^6 |l_i - l_{av}| / (6l_{av})$ and the *bond angle variance* $\mathbf{S} = \sum_{i=1}^8 (\phi_i - 90^\circ)^2 / 722$. Here l_i and ϕ_i are the bond distances and bond-angles, respectively. l_{av} is the average bond length. \mathbf{D} and \mathbf{S} are zero for an ideal octahedra.

At all temperatures and in both compounds t_{2g} electrons are in the Mott insulating state, and remain gapped even in the high temperature metallic phase (see Figs. 2 and 3). This can be verified by looking at the t_{2g} self-energy, which has a pole inside the gap even when the e_g density of states shows metallic behavior (see online materials F to H). This state is commonly called *orbital-selective Mott state*⁵³⁻⁵⁵, and was first introduced in Ref. 53 to explain the properties of Ca_{2-x}Sr_xRuO₄ in which spin-1/2 local moments coexist with metallic transport. Such a picture of *frozen high-spin* t_{2g} electrons in LaMnO₃ was postulated already in the very early works on the double-exchange model⁵⁶⁻⁵⁸, and was also assumed in the previous DMFT calculations within the minimal two orbital Hubbard model^{49,50}. In the limit of

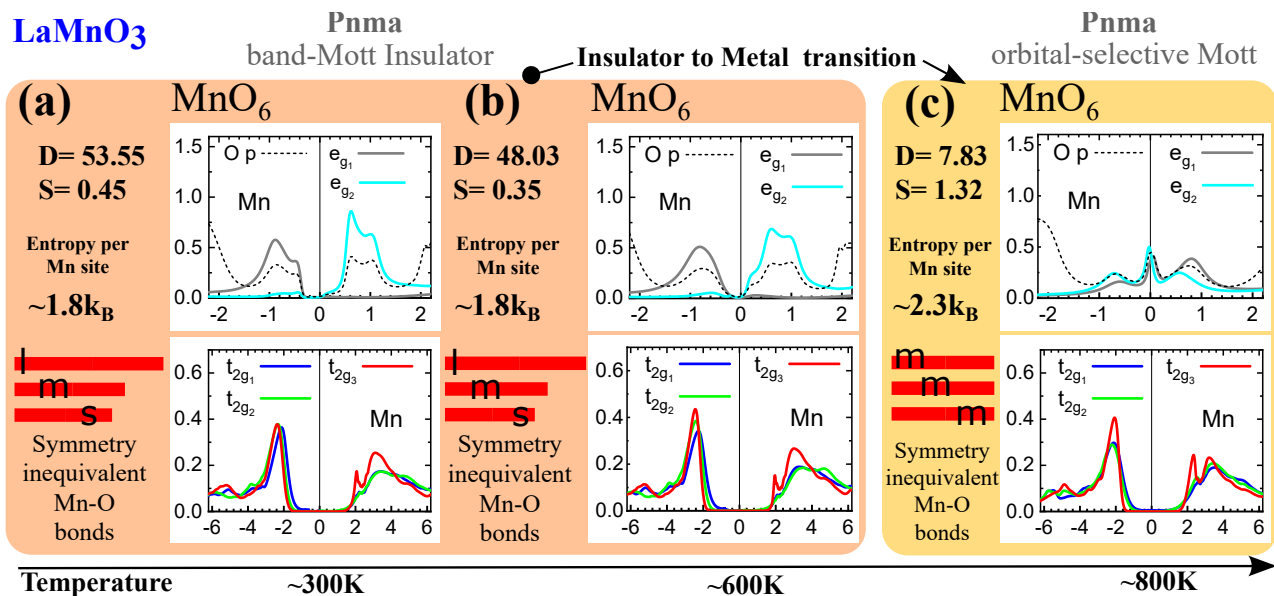


FIG. 2: **Temperature dependent electronic states in LaMnO_3** : Panels (a) to (c) show for each inequivalent Mn octahedra the following properties: (1) values of the distortion indices, \mathbf{D} and \mathbf{S} ; (2) electronic entropy per Mn site; (3) schematic view of the symmetry inequivalent Mn-O bonds represented by red horizontal bars (the horizontal size of the bar is proportional with the bond length, short-s, medium-m, long-l); (4) e_g and t_{2g} projected density of states per formula unit versus energy in eV, for each electronic phase at a given temperature. On top of each panel we give the crystallographic symmetry at a given temperature and a name characterizing the electronic properties of the predicted electronic phases. The panels are connected by arrows suggesting the order parameter of the phase transitions.

weak correlations among e_g electrons, coexisting with the *high-spin core* t_{2g} states, the DMFT problem maps to the ferromagnetic Kondo model, which was shown in Ref. 59 to explain qualitatively the giant magnetoresistance in doped LaMnO_3 . Nevertheless, to the best of our knowledge, direct DMFT simulations with equal dynamic treatment of both t_{2g} and e_g orbitals was lacking, hence the theoretical photoemission spectra and position of the t_{2g} states was unknown. Moreover, as we will see in BiMnO_3 the approximation of t_{2g} electrons as *frozen high-spin core* is not really adequate.

Fig. 2a shows that the room temperature gap is between e_g states, in which the occupied part is strongly admixed with oxygen states. The orbital with larger occupation (e_{g1}) points along the longest Mn-O bond, while the less occupied orbital (e_{g2}) points towards the shorter bonds. The gap between e_g 's is not of Mott type, hence we call this state *band-Mott insulator*. The peak-to-peak splitting between these low-energy states is between 1.8 – 2 eV in the orbital ordered state, and the gap collapses around 800 K in the high-temperature orthorhombic structure, in which the three Mn-O bonds become very similar, although not strictly equal. Consequently, the two e_g orbitals are close to degenerate, but still different (see Fig. 2c). The phase-transition around 800 K is thus a first order metal-insulator transition, strongly coupled with the structural evolution in which the distortion of the octahedra is strongly reduced, but the symmetry of

the crystal structure does not change. This calculation shows not only that the details of the crystal structure and the lattice distortions have large impact on the electronic state, but also that the feedback effect of the electronic correlations on the crystal structure is crucial to properly describe the temperature evolution of the system. To understand whether structural distortions or electronic correlations drive the transition, we also calculate the electronic entropy⁶⁰ per Mn-site at three temperatures as shown in Fig. 2. While normally the metallic phase has small entropy, and the Mott insulating state carries large entropy, here the situation is very different. In the insulating state we find the entropy to be around $1.8 k_B$ per Mn-site, while in the bad-metallic state it is increased to $2.3 k_B$, which corresponds to 35 meV entropy gain across the transition, which is a decisive contribution to the free energy for the metal-insulator transition.

The important consequence of the Mott insulating t_{2g} states coexisting with the metallic e_g states at high temperature in the existence of so-called *orbital-selective Mott state* (OSM), in which e_g electrons have enormous scattering rate (of the order of eV), and consequently small mobility so that there are no real bands present in the photoemission spectra, but rather just a very incoherent spectral weight (see Fig. 4). Photoemission on LaMnO_3 revealed that the system is of charge transfer-type insulator, with strong admixture of oxygen p and Mn- e_g weight around 1 eV below the Fermi level⁵¹. In

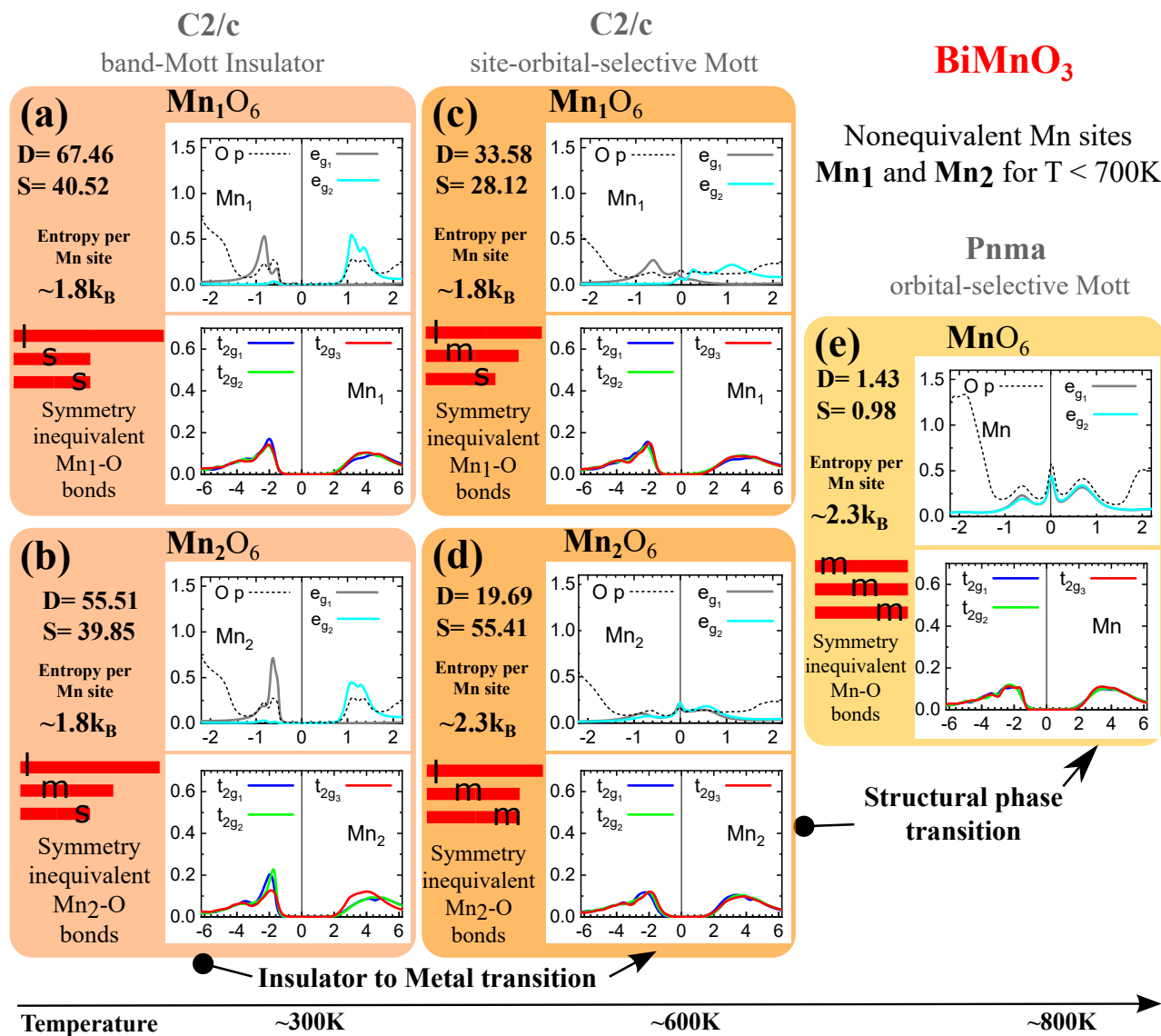


FIG. 3: **Temperature dependent electronic states in BiMnO₃**: Panels (a) to (e) show for each inequivalent Mn octahedra the following properties: (1) values of the distortion indices, **D** and **S**; (2) electronic entropy per Mn site; (3) schematic view of the symmetry inequivalent Mn-O bonds represented by red horizontal bars (the horizontal size of the bar is proportional with the bond length, short-s, medium-m, long-l); (4) e_g and t_{2g} projected density of states per formula unit versus energy in eV, for each electronic phase at a given temperature. On top of each panel we give the crystallographic symmetry at a given temperature and a name characterizing the electronic properties of the predicted electronic phases. The panels are connected by arrows suggesting the order parameter of the phase transitions.

Ref. 61 a strong peak at approximately -3eV and a shoulder between -1.5eV and the fermi level was identified, which we now interpret as the t_{2g} and e_g peak in the density of states, respectively. Even more revealing are optical experiments, which show strong temperature dependent peak around 2eV present only in the orbitally ordered state⁶², and replaced by broad distribution of optical weight above 800K . By analyzing low temperature data in Ref. 63 it was found that the 2eV peak in optics comes from $e_g - e_g$ transitions, and that $t_{2g} - e_g$ tran-

sitions appear at 3.8eV . This is all consistent with our spectra in Fig. 2a, as the $e_g - e_g$ distance is close to 2eV and the $t_{2g} - e_g$ distance is close to 4eV at room temperature, while in disordered state above 800K the gap disappears and the scattering rate broadens low energy excitations. We note that in earlier DMFT works, the $e_g - e_g$ splitting in the ordered state was somewhat too large ($\approx 3.5\text{eV}$ ⁴⁹ and $\approx 4\text{eV}$ ⁵⁰), pointing again to the shortcomings of the low energy Hubbard-type modeling. Finally we note that theoretical DOS in Fig. 2 are plot-

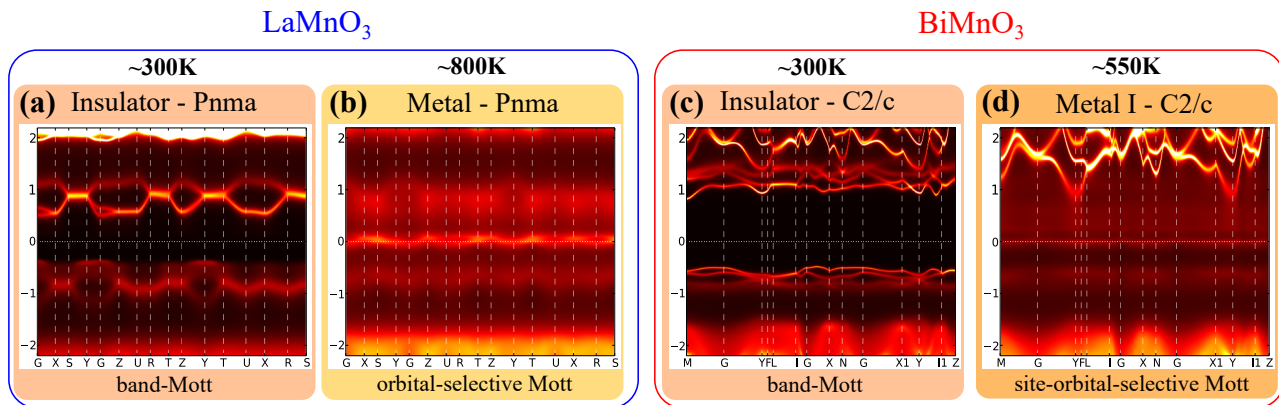


FIG. 4: **Spectral functions for various novel phases in (Bi,La)MnO₃**: For both compounds we give the spectral functions showing the metal to insulator phase transitions. In panels (a) and (b) we show the spectral functions for the *band-Mott* and *orbital-selective Mott* states for LaMnO₃; in panels (c) and (d) we show the spectral functions of the *band-Mott* and *site-orbital-selective Mott* states for BiMnO₃.

ted using experimental crystal structures, but the results do not change appreciably when the theoretical crystal structures are used.

While large amount of experimental data is available for LaMnO₃, very little is known about BiMnO₃. Our calculations (Fig. 3) show strong similarity with LaMnO₃, but also some important differences.

In particular, there is stronger anisotropy within the DOS of the t_{2g} and e_g orbitals for the Mn₂-ion compared to the Mn₁-ion (see Fig. 3a and b). For example, there is a very sharp peak in the DOS of two t_{2g} orbitals at -2.0 eV and e_g orbital at -0.6 eV, corresponding to Mn₂-ion (Fig. 3b). This is a consequence of the anisotropic hybridization between the lone-pair, O-p and Mn₂-d orbitals. We recall that the lone-pair of Bi-6s state points towards the face of the distorted Mn₂O₆ octahedra as shown in Fig. 1d, thus this anisotropic hybridization is present in the system (see online materials I). The anisotropic hybridization of the t_{2g} orbitals with the lone-pair in the case of Mn₂ atoms is also confirmed by the fact that the Mn₁ atoms have similar distortions, but the corresponding DOS of the t_{2g} orbitals is isotropic (Fig. 3a). The highly distorted monoclinic crystal structure of BiMnO₃ compound, is a consequence of the competition between the Jahn-Teller octahedra distortions that are squeezing the lone-pair of Bi-6s state. This is different from the case of LaMnO₃ compound, where the lone-pair is absent, thus the Jahn-Teller octahedra distortions appears in the orthorhombic crystal structure.

At room temperature, the local Jahn-Teller distortions for both inequivalent Mn ions are large enough to decrease the e_{g1} hybridization with the O-p states allowing localization of e_g electrons, even though the e_g orbitals also hybridize with the lone-pair. These local distortions are depicted by red segments and given in terms of distortion indices in Fig. 3a and b.

Note that larger values of the bond distortion index \mathbf{D} in octahedra corresponds to more anisotropic hybridiza-

tion between the two e_g orbitals and O-p states, causing orbital polarization and consequently localization of electrons. With increasing temperature our theoretical method reveals that the local Jahn-Teller distortions decrease (meaning smaller \mathbf{D} values), thus the e_{g1} hybridization with the O-p states is increasing while the e_{g2} hybridization is decreasing (see online materials J). At the same time the lone-pair is exerting pressure on the neighboring ions to gain more space, thus it is contributing further to decreasing local distortions. Since the lone-pair points towards the face of the Mn₂O₆ distorted octahedra, the local distortions of the Mn₂ site get reduced faster with increasing temperature then for the Mn₁ site. These local distortions are depicted by red segments and given in terms of distortion indices in Fig. 3c and d. Consequently, when the local distortions are small enough, e_{g1} and e_{g2} hybridization with the O-p states become similar, thus the e_g gap on Mn₂ ion collapses, and the system becomes bad metal. While decreasing the local distortions, the anisotropic hybridization of the t_{2g} with the lone-pair and O-p orbitals disappears, i.e., the resonance in t_{2g} DOS disappears going from Fig. 3b to d. However, Mn₁ ion remains close to its low-temperature state, for one thing, its orbital occupancy in Table 1 remains unchanged, and the e_g states show DOS with a pseudogap (Fig. 3c). We call this state *site-orbital-selective Mott* state, and we note that the orbital order remains strong only on Mn₁ ion. Such partial orbital order on half of Mn ions is consistent with RXS experiments⁴³, in which the room temperature signal was roughly factor of two stronger than in the intermediate state. Surprisingly, the entropy on Mn atoms is very weakly temperature dependent between the room temperature and the first transition (around 600 K), at which the entropy on Mn₂ increases for $0.5 k_B$, while the entropy on Mn₁ remains almost unchanged. Only at the second transition around 800 K the entropy of Mn₁ increases to its saturated value within the bad metallic state.

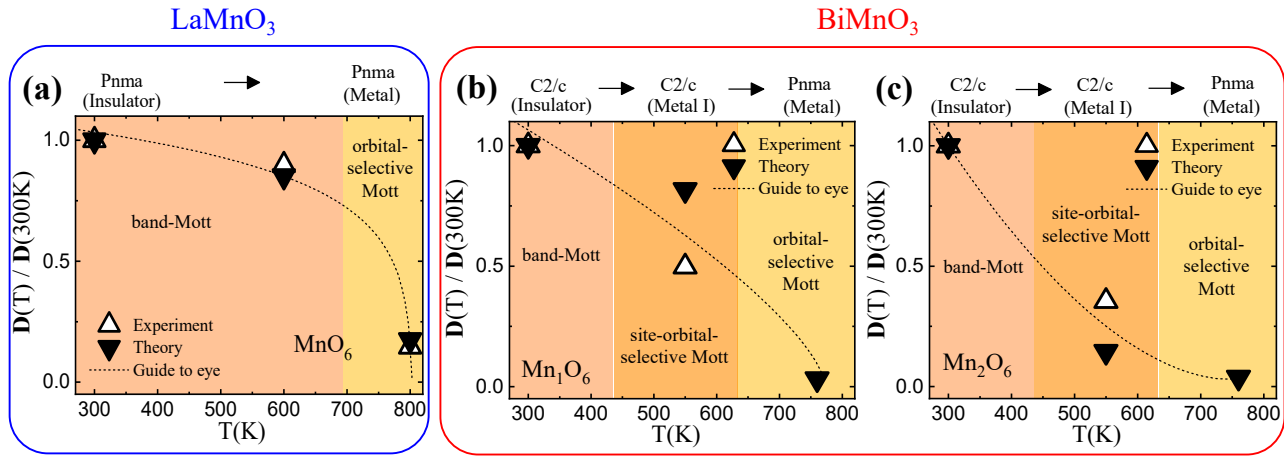


FIG. 5: **Structural relaxations within LDA+eDMFT for all the temperature dependent novel electronic phases in (Bi,La)MnO₃**: In each panel we plot the Bond Distortion (\mathbf{D}) index versus temperature, normalized to its values at room temperature. In panel (a) we plot \mathbf{D} for the Mn site in LaMnO₃. In panels (b) and (c) we plot \mathbf{D} for the two inequivalent Mn sites in BiMnO₃. Above each panel we give the temperature dependent crystal symmetry and the properties of that electronic state (metal or insulator). The arrows point to the type of phase transition (structural or metal-insulator phase transition).

We also note that the electronic spectral weight of the t_{2g} orbitals pointing towards the lone-pair is strongly temperature dependent, therefore treating t_{2g} electrons as a fixed core spin would not result in correct prediction of the crystal structures.

Fig. 4 displays the single-particle spectral functions $A(\mathbf{k}, \omega)$ in the insulating room temperature state, and in the first metallic state. The room temperature direct gap in LaMnO₃ and BiMnO₃ are ≈ 0.8 eV and 1.2 eV, which are in decent agreement with optical experiments (0.9 eV in LaMnO₃⁶² and 1.2 eV in BiMnO₃^{64,65}). We note that the prediction of the gap size in BiMnO₃ seems to be very challenging for other ab-initio methods, as the gap size is either too large (hybrid functional 1.7 eV²⁸) or too small (modified Becke-Johnson exchange functional 0.75 eV⁶⁶; 0.5 eV or less by various LDA+U calculations⁶⁷⁻⁷⁰). Finally, the *orbital-selective Mott* phase, in which the orbital order is melted away, is displayed in Fig. 4b. The spectral functions has no sharp bands, only the incoherent spectral weight, hence the charge mobility is very low. This state is also realized in the ferromagnetic Kondo model of Ref. 59, therefore it might show giant magnetoresistance. Fig. 4d shows the new phase *site-orbital-selective Mott* state, realized in the intermediate temperature range where Mn₁ shows orbital ordering and Mn₂ does not. This state is a superposition of very incoherent *orbital-selective Mott* phase and the insulating phase, which shows somewhat more sharp bands above 1 eV.

Fig. 5 shows the comparison between the theoretical and experimental temperature dependence of the distortion index \mathbf{D} . In LaMnO₃ it changes only for 20% between the room temperature and 550 K, while it collapses abruptly around 800 K. We note an excellent agreement between the theoretical and experimental distortion in-

dex. In BiMnO₃ the two Mn sites show very different behaviour: the changes on Mn₁ are comparable to LaMnO₃ (20%), while on Mn₂ ion the distortion is almost complete at 550 K (80%). In the high temperature phase the distortion is small but finite. The reason for such markedly different behaviour of the two sites is that Mn₂ ion hybridizes with the Bi 6s lone-pair, while Mn₁ does not. Finally, we note that the measured and theoretical distortion index have similar trend, except that the disproportionation between Mn₁ and Mn₂ seems a bit weaker in experiment than in theory.

In conclusion, using eDMFT methods we found novel electronic state in Mn perovskite system, such as *site-orbital-selective Mott* state, which hosts Mott insulating t_{2g} states, and a combination of semi-metallic and metallic e_g states on two inequivalent Mn atoms. We showed that the isostructural transition in BiMnO₃ at 474 K should be characterized as the insulator-metal transition at which half of Mn atoms give up the orbital order, while the fully disordered state is reached only at the structural transition of 768 K. We showed that the electronic entropy plays the decisive role in the metal-insulator transition in both compounds. By self-consistent determination of both the correlated electronic state and the corresponding relaxed crystal structure we showed that the temperature evolution of phases in LaMnO₃ and BiMnO₃ can be properly explained from first principles, thus demonstrating the predictive power of the eDMFT method for structural and electronic properties. In addition, we predict the temperature dependence of the spectral functions for the novel phases found in Mn perovskite systems, predictions that can be tested experimentally by ARPES.

Acknowledgements

G.L.P. was supported by the U.S. Department of Energy, Office of Science, Basic Energy Sciences, as a part of the Computational Materials Science Program, funded by the U.S. Department of Energy, Office of Science, Basic Energy Sciences, Materials Sciences and Engineering Division. K.H. was supported by the NSF DMR-1709229.

Author contributions

G.L.P. carried out the calculations. K.H. developed the code. G.L.P and K.H. analyzed the results and wrote the

paper.

Competing financial interests

The authors declare no competing interests.

-
- ¹ Dagotto, E., Hotta, T. & Moreo, A. Colossal magnetoresistant materials: the key role of phase separation. *Physics Reports* **344**, 1 – 153 (2001). URL <http://www.sciencedirect.com/science/article/pii/S0370157300001216>.
- ² Ramirez, A. P. Colossal magnetoresistance. *Journal of Physics: Condensed Matter* **9**, 8171 (1997). URL <http://stacks.iop.org/0953-8984/9/i=39/a=005>.
- ³ Imada, M., Fujimori, A. & Tokura, Y. Metal-insulator transitions. *Rev. Mod. Phys.* **70**, 1039–1263 (1998). URL <https://link.aps.org/doi/10.1103/RevModPhys.70.1039>.
- ⁴ Khomskii, D. Multiferroics: Different ways to combine magnetism and ferroelectricity. *Journal of Magnetism and Magnetic Materials* **306**, 1 – 8 (2006). URL <http://www.sciencedirect.com/science/article/pii/S0304885306004239>.
- ⁵ Tokura, Y. & Nagaosa, N. Orbital physics in transition-metal oxides. *Science* **288**, 462–468 (2000). URL <http://science.sciencemag.org/content/288/5465/462>.
- ⁶ DFT + Embedded DMFT functional. <http://hauleweb.rutgers.edu/tutorials/>, where for the DFT part we are using the WIEN2k code: P. Blaha, K. Schwarz, G. K. H. Madsen, D. Kvasnicka, J. Luitz, R. Laskowski, F. Tran and L. D. Marks, WIEN2k, An Augmented Plane Wave + Local Orbitals Program for Calculating Crystal Properties (Karlheinz Schwarz, Techn. Universität Wien, Austria), 2018. ISBN 3-9501031-1-2.
- ⁷ Haule, K., Yee, C.-H. & Kim, K. Dynamical mean-field theory within the full-potential methods: Electronic structure of CeIrIn₅, CeCoIn₅, and CeRhIn₅. *Phys. Rev. B* **81**, 195107 (2010). URL <http://link.aps.org/doi/10.1103/PhysRevB.81.195107>.
- ⁸ Haule, K. Structural predictions for correlated electron materials using the functional dynamical mean field theory approach. *Journal of the Physical Society of Japan* **87**, 041005 (2018). URL <https://doi.org/10.7566/JPSJ.87.041005>. <https://doi.org/10.7566/JPSJ.87.041005>.
- ⁹ Shim, J. H., Haule, K. & Kotliar, G. Fluctuating valence in a correlated solid and the anomalous properties of delta-plutonium. *Nature* **446**, 513 (2007). URL <http://dx.doi.org/10.1038/nature05647>.
- ¹⁰ Janoschek, M. et al. The valence-fluctuating ground state of plutonium. *Science Advances* **1** (2015). URL <http://advances.sciencemag.org/content/1/6/e1500188>.
- ¹¹ Mandal, S., Cohen, R. E. & Haule, K. Strong pressure-dependent electron-phonon coupling in FeSe. *Phys. Rev. B* **89**, 220502 (2014). URL <https://link.aps.org/doi/10.1103/PhysRevB.89.220502>.
- ¹² Gerber, S. et al. Femtosecond electron-phonon lock-in by photoemission and x-ray free-electron laser. *Science* **357**, 71–75 (2017). URL <http://science.sciencemag.org/content/357/6346/71>.
- ¹³ Yin, Z. P., Haule, K. & Kotliar, G. Kinetic frustration and the nature of the magnetic and paramagnetic states in iron pnictides and iron chalcogenides. *Nat Mater* **10**, 932 (2011). URL <http://dx.doi.org/10.1038/nmat3120>.
- ¹⁴ Liu, M. et al. Nature of magnetic excitations in superconducting BaFe_{1.9}Ni_{0.1}As₂. *Nature Physics* **8**, 376 EP – (2012). URL <https://doi.org/10.1038/nphys2268>.
- ¹⁵ Ohta, K. et al. Experimental and theoretical evidence for pressure-induced metallization in FeO with rocksalt-type structure. *Phys. Rev. Lett.* **108**, 026403 (2012). URL <http://link.aps.org/doi/10.1103/PhysRevLett.108.026403>.
- ¹⁶ Haule, K. & Kotliar, G. Arrested kondo effect and hidden order in URu₂Si₂. *Nat Phys* **5**, 796 (2009). URL <http://dx.doi.org/10.1038/nphys1392>.
- ¹⁷ Kung, H.-H. et al. Chirality density wave of the “hidden order” phase in URu₂Si₂. *Science* **347**, 1339–1342 (2015). URL <http://science.sciencemag.org/content/347/6228/1339>.
- ¹⁸ Haule, K. & Pascut, G. L. Forces for structural optimizations in correlated materials within a DFT+embedded DMFT functional approach. *Phys. Rev. B* **94**, 195146 (2016). URL <https://link.aps.org/doi/10.1103/PhysRevB.94.195146>.
- ¹⁹ Haule, K. & Pascut, G. L. Mott transition and magnetism in rare earth nickelates and its fingerprint on the X-ray scattering. *Scientific Reports* **7**, 10375 (2017). URL <https://doi.org/10.1038/s41598-017-10374-2>.
- ²⁰ Stanislavchuk, T. N. et al. Spectroscopic and first principle DFT+eDMFT study of complex structural, electronic, and vibrational properties of M₂Mo₃O₈ (M=Fe, Mn) polar magnets. arXiv:1902.02325 (2019).
- ²¹ Seshadri, R. & Hill, N. A. Visualizing the role of bi 6s lone pairs in the off-center distortion in ferromagnetic BiMnO₃. *Chemistry of Materials* **13**, 2892–2899 (2001). URL <http://dx.doi.org/10.1021/cm01050a021>.

- //dx.doi.org/10.1021/cm010090m.
- 22 Momma, K. & Izumi, F. *VESTA3* for three-dimensional visualization of crystal, volumetric and morphology data. *Journal of Applied Crystallography* **44**, 1272–1276 (2011). URL <https://doi.org/10.1107/S0021889811038970>.
 - 23 Baldini, M., Struzhkin, V. V., Goncharov, A. F., Postorino, P. & Mao, W. L. Persistence of Jahn-Teller distortion up to the Insulator to Metal Transition in LaMnO_3 . *Phys. Rev. Lett.* **106**, 066402 (2011). URL <https://link.aps.org/doi/10.1103/PhysRevLett.106.066402>.
 - 24 Thygesen, P. M. M. et al. Local structure study of the orbital order/disorder transition in LaMnO_3 . *Phys. Rev. B* **95**, 174107 (2017). URL <https://link.aps.org/doi/10.1103/PhysRevB.95.174107>.
 - 25 Chou, C. C. et al. Multiple magnetic transitions in multiferroic BiMnO_3 . *Phys. Rev. B* **80**, 184426 (2009). URL <https://link.aps.org/doi/10.1103/PhysRevB.80.184426>.
 - 26 Belik, A. A. & Takayama-Muromachi, E. Effects of doping on structural, physical, and chemical properties of multiferroic BiMnO_3 and BiCrO_3 . *Transactions of the Materials Research Society of Japan* **34**, 39–42 (2009).
 - 27 Belik, A. A. Polar and nonpolar phases of BiMO_3 : A review. *Journal of Solid State Chemistry* **195**, 32 – 40 (2012). URL <http://www.sciencedirect.com/science/article/pii/S0022459612000394>.
 - 28 Diéguez, O. & Íñiguez, J. Epitaxial phases of bimno_3 from first principles. *Phys. Rev. B* **91**, 184113 (2015). URL <https://link.aps.org/doi/10.1103/PhysRevB.91.184113>.
 - 29 Kimura, T. et al. Magnetocapacitance effect in multiferroic BiMnO_3 . *Phys. Rev. B* **67**, 180401 (2003). URL <https://link.aps.org/doi/10.1103/PhysRevB.67.180401>.
 - 30 Belik, A. A., Kolodiazny, T., Kosuda, K. & Takayama-Muromachi, E. Synthesis and properties of oxygen non-stoichiometric BiMnO_3 . *J. Mater. Chem.* **19**, 1593–1600 (2009). URL <http://dx.doi.org/10.1039/B818645F>.
 - 31 Rodríguez-Carvajal, J. et al. Neutron-diffraction study of the Jahn-Teller transition in stoichiometric LaMnO_3 . *Phys. Rev. B* **57**, R3189–R3192 (1998). URL <https://link.aps.org/doi/10.1103/PhysRevB.57.R3189>.
 - 32 Zhou, J.-S. & Goodenough, J. B. Paramagnetic phase in single-crystal LaMnO_3 . *Phys. Rev. B* **60**, R15002–R15004 (1999). URL <https://link.aps.org/doi/10.1103/PhysRevB.60.R15002>.
 - 33 Souza, J. A. et al. Magnetic susceptibility and electrical resistivity of LaMnO_3 , CaMnO_3 , and $\text{La}_{1-x}\text{Sr}_x\text{MnO}_3$ ($0.13 \leq x \leq 0.45$) in the temperature range 300 – 900K. *Phys. Rev. B* **76**, 024407 (2007). URL <https://link.aps.org/doi/10.1103/PhysRevB.76.024407>.
 - 34 Ramirez, F. et al. Structural, electronic, and magnetic entropy contributions of the orbital order/disorder transition in LaMnO_3 . *Phase Transitions* **84**, 284–290 (2011). URL <http://dx.doi.org/10.1080/01411594.2010.534656>.
 - 35 Mandal, P., Bandyopadhyay, B. & Ghosh, B. Resistivity anomaly in the vicinity of a structural phase transition in $\text{La}_{1-x}\text{Sr}_x\text{MnO}_3$. *Phys. Rev. B* **64**, 180405 (2001). URL <https://link.aps.org/doi/10.1103/PhysRevB.64.180405>.
 - 36 Belik, A. A. et al. Origin of the monoclinic-to-monoclinic phase transition and evidence for the centrosymmetric crystal structure of BiMnO_3 . *Journal of the American Chemical Society* **129**, 971–977 (2007). URL <http://dx.doi.org/10.1021/ja0664032>.
 - 37 Yokosawa, T. et al. Crystal symmetry of BiMnO_3 : Electron diffraction study. *Phys. Rev. B* **77**, 024111 (2008). URL <https://link.aps.org/doi/10.1103/PhysRevB.77.024111>.
 - 38 Toulemonde, P., Bordet, P., Bouvier, P. & Kreisel, J. Single-crystalline BiMnO_3 studied by temperature-dependent x-ray diffraction and raman spectroscopy. *Phys. Rev. B* **89**, 224107 (2014). URL <https://link.aps.org/doi/10.1103/PhysRevB.89.224107>.
 - 39 Krüger, R. et al. Orbital ordering in LaMnO_3 investigated by resonance raman spectroscopy. *Phys. Rev. Lett.* **92**, 097203 (2004). URL <https://link.aps.org/doi/10.1103/PhysRevLett.92.097203>.
 - 40 Solovyev, I. V. & Pchelkina, Z. V. Orbital ordering and magnetic interactions in BiMnO_3 . *New Journal of Physics* **10**, 073021 (2008). URL <http://stacks.iop.org/1367-2630/10/i=7/a=073021>.
 - 41 Colella, R. & Shen, Q. Resonant scattering and multiple Bragg X-ray diffraction in LaMnO_3 ; a classical view. *Acta Crystallographica Section A* **62**, 459–462 (2006). URL <https://doi.org/10.1107/S010876730603889X>.
 - 42 Murakami, Y. et al. Resonant x-ray scattering from orbital ordering in LaMnO_3 . *Phys. Rev. Lett.* **81**, 582–585 (1998). URL <https://link.aps.org/doi/10.1103/PhysRevLett.81.582>.
 - 43 Yang, C.-H. et al. Resonant x-ray scattering study on multiferroic BiMnO_3 . *Phys. Rev. B* **73**, 224112 (2006). URL <https://link.aps.org/doi/10.1103/PhysRevB.73.224112>.
 - 44 Sawada, H., Morikawa, Y., Terakura, K. & Hamada, N. Jahn-Teller distortion and magnetic structures in LaMnO_3 . *Phys. Rev. B* **56**, 12154–12160 (1997). URL <https://link.aps.org/doi/10.1103/PhysRevB.56.12154>.
 - 45 Hashimoto, T., Ishibashi, S. & Terakura, K. Jahn-Teller distortion and magnetic structure in LaMnO_3 : A first-principles theoretical study with full structure optimizations. *Phys. Rev. B* **82**, 045124 (2010). URL <https://link.aps.org/doi/10.1103/PhysRevB.82.045124>.
 - 46 Boukhvalov, D. W. & Solovyev, I. V. Defects of the crystal structure and Jahn-Teller distortion in BiMnO_3 . *Phys. Rev. B* **82**, 245101 (2010). URL <https://link.aps.org/doi/10.1103/PhysRevB.82.245101>.
 - 47 Ahmed, M. R. & Gehring, G. A. Volume collapse in LaMnO_3 studied using an anisotropic potts model. *Phys. Rev. B* **79**, 174106 (2009). URL <https://link.aps.org/doi/10.1103/PhysRevB.79.174106>.
 - 48 Glazkova, Y. S., Belik, A. A., Sobolev, A. V. & Presniakov, I. A. Local crystal structure of multiferroic BiMnO_3 studied by ^{57}Fe probe mössbauer spectroscopy. *Inorganic Materials* **52**, 499–503 (2016). URL <https://doi.org/10.1134/S0020168516050058>.
 - 49 Pavarini, E. & Koch, E. Origin of Jahn-Teller distortion and orbital order in LaMnO_3 . *Phys. Rev. Lett.* **104**, 086402 (2010). URL <https://link.aps.org/doi/10.1103/PhysRevLett.104.086402>.
 - 50 Leonov, I., Korotin, D., Binggeli, N., Anisimov, V. I. & Vollhardt, D. Computation of correlation-induced atomic displacements and structural transformations in paramagnetic KCuF_3 and LaMnO_3 . *Phys. Rev. B* **81**, 075109 (2010). URL <https://link.aps.org/doi/10.1103/PhysRevB.81.075109>.

- ⁵¹ Saitoh, T. et al. Electronic structure of $\text{La}_{1-x}\text{Sr}_x\text{MnO}_3$ studied by photoemission and x-ray-absorption spectroscopy. *Phys. Rev. B* **51**, 13942–13951 (1995). URL <https://link.aps.org/doi/10.1103/PhysRevB.51.13942>.
- ⁵² Haule, K. Exact double counting in combining the dynamical mean field theory and the density functional theory. *Phys. Rev. Lett.* **115**, 196403 (2015). URL <http://link.aps.org/doi/10.1103/PhysRevLett.115.196403>.
- ⁵³ Anisimov, V., Nekrasov, I. & Kondakov, D. e. Orbital-selective Mott-insulator transition in $\text{Ca}_{2-x}\text{Sr}_x\text{RuO}_4$. *Eur. Phys. J. B* **25**, 191 (2002). URL <https://doi.org/10.1140/epjb/e20020021>.
- ⁵⁴ de’Medici, L., Georges, A. & Biermann, S. Orbital-selective mott transition in multiband systems: Slave-spin representation and dynamical mean-field theory. *Phys. Rev. B* **72**, 205124 (2005). URL <https://link.aps.org/doi/10.1103/PhysRevB.72.205124>.
- ⁵⁵ Georges, A., Medici, L. d. & Mravlje, J. Strong correlations from hunds coupling. *Annual Review of Condensed Matter Physics* **4**, 137–178 (2013). URL <https://doi.org/10.1146/annurev-commatphys-020911-125045>.
- ⁵⁶ Zener, C. Interaction between the d -shells in the transition metals. ii. ferromagnetic compounds of manganese with perovskite structure. *Phys. Rev.* **82**, 403–405 (1951). URL <https://link.aps.org/doi/10.1103/PhysRev.82.403>.
- ⁵⁷ Anderson, P. W. & Hasegawa, H. Considerations on double exchange. *Phys. Rev.* **100**, 675–681 (1955). URL <https://link.aps.org/doi/10.1103/PhysRev.100.675>.
- ⁵⁸ de Gennes, P. G. Effects of double exchange in magnetic crystals. *Phys. Rev.* **118**, 141–154 (1960). URL <https://link.aps.org/doi/10.1103/PhysRev.118.141>.
- ⁵⁹ Furukawa, N. Transport properties of the kondo lattice model in the limit $S=\infty$ and $D=\infty$. *Journal of the Physical Society of Japan* **63**, 3214–3217 (1994). URL <https://doi.org/10.1143/JPSJ.63.3214>.
- ⁶⁰ Haule, K. & Birol, T. Free energy from stationary implementation of the DFT + DMFT functional. *Phys. Rev. Lett.* **115**, 256402 (2015). URL <http://link.aps.org/doi/10.1103/PhysRevLett.115.256402>.
- ⁶¹ Park, J.-H. et al. Electronic aspects of the ferromagnetic transition in manganese perovskites. *Phys. Rev. Lett.* **76**, 4215–4218 (1996). URL <https://link.aps.org/doi/10.1103/PhysRevLett.76.4215>.
- ⁶² Tobe, K., Kimura, T., Okimoto, Y. & Tokura, Y. Anisotropic optical spectra in a detwinned LaMnO_3 crystal. *Phys. Rev. B* **64**, 184421 (2001). URL <https://link.aps.org/doi/10.1103/PhysRevB.64.184421>.
- ⁶³ Kovaleva, N. N. et al. Spin-controlled mott-hubbard bands in LaMnO_3 probed by optical ellipsometry. *Phys. Rev. Lett.* **93**, 147204 (2004). URL <https://link.aps.org/doi/10.1103/PhysRevLett.93.147204>.
- ⁶⁴ Lee, J. H. et al. Adsorption-controlled growth of BiMnO_3 films by molecular-beam epitaxy. *Applied Physics Letters* **96**, 262905 (2010). URL <https://doi.org/10.1063/1.3457786>.
- ⁶⁵ Xu, X. S. et al. Tunable band gap in $\text{Bi}(\text{Fe}_{1-x}\text{Mn}_x)\text{O}_3$ films. *Applied Physics Letters* **96**, 192901 (2010). URL <https://doi.org/10.1063/1.3427499>.
- ⁶⁶ Zhu, X., Chen, X. & Liu, B. First principles investigation of electronic and magnetic structures of centrosymmetric BiMnO_3 using an improved approach. *Solid State Communications* **243**, 65 – 70 (2016). URL <http://www.sciencedirect.com/science/article/pii/S0038109816301235>.
- ⁶⁷ Mei, Z.-G., Shang, S.-L., Wang, Y. & Liu, Z.-K. First-principles study of structural and elastic properties of monoclinic and orthorhombic BiMnO_3 . *Journal of Physics: Condensed Matter* **22**, 295404 (2010). URL <http://stacks.iop.org/0953-8984/22/i=29/a=295404>.
- ⁶⁸ McLeod, J. A. et al. Electronic structure of BiMO_3 multiferroics and related oxides. *Phys. Rev. B* **81**, 144103 (2010). URL <https://link.aps.org/doi/10.1103/PhysRevB.81.144103>.
- ⁶⁹ Bi, L. et al. Structural, magnetic, and optical properties of BiFeO_3 and $\text{Bi}_2\text{FeMnO}_6$ epitaxial thin films: An experimental and first-principles study. *Phys. Rev. B* **78**, 104106 (2008). URL <https://link.aps.org/doi/10.1103/PhysRevB.78.104106>.
- ⁷⁰ Shishidou, T., Mikamo, N., Uratani, Y., Ishii, F. & Oguchi, T. First-principles study on the electronic structure of bismuth transition-metal oxides. *Journal of Physics: Condensed Matter* **16**, S5677 (2004). URL <http://stacks.iop.org/0953-8984/16/i=48/a=026>.